Revision 2

Compressibility, thermal expansion and Raman scattering of synthetic whitlockite $Ca_9Mg(PO_3OH)(PO_4)_6$ at high pressures and high temperatures

Word count: 6443

Muhua Jia[a], Yungui Liu[b], Sheng Jiang[c], Wen Wen[c], Shuangmeng Zhai[a, *]

[a]Key Laboratory of High-temperature and High-pressure Study of the Earth's Interior, Institute of Geochemistry, Chinese Academy of Sciences, Guiyang 550081, China

[b]State Key Laboratory of Geological Processes and Mineral Resources, China University of Geosciences, Wuhan 430074, China

[c]Shanghai Synchrotron Radiation Facility, Shanghai Advanced Research Institute, Chinese Academy of Sciences, Shanghai 201210, China

*Correspondence to:

S. Zhai, Institute of Geochemistry, Chinese Academy of Sciences, Guiyang, Guizhou 550081, China

Tel: +86-851-84390656 Email: zhaishuangmeng@mail.gyig.ac.cn

Abstract In-situ X-ray diffraction and Raman scattering of synthetic whitlockite, $Ca_9Mg(PO_3OH)(PO_4)_6$, have been systematically measured at high pressures and high temperatures, respectively. The results show that whitlockite is stable up to ~ 15 GPa at ambient temperature and undergoes a temperature-induced dehydrogenation to merrillite above 973 K at ambient pressure. The obtained pressure-volume data were fitted using a third-order Birch-Murnaghan equation of state to yield the isothermal bulk modulus as K_0 = 79(4) GPa with pressure derivative K_0' = 4.3(6). When K_0' was fixed at 4, the refined isothermal bulk modulus was 81(1) GPa. The volumetric thermal expansion coefficient (α_V) is equal to 4.05(8) × 10^{-5} K^{-1}. The axial thermal expansion coefficients (α_a and α_c) are 1.07(5) × 10^{-5} K^{-1} and 1.91(6) × 10^{-5} K^{-1}. Both compressibility and thermal expansion show an axial anisotropy. The effects of pressure and temperature on the Raman spectra of whitlockite have been quantitatively analyzed. The isothermal and isobaric mode Grüneisen parameters, and the intrinsic anharmonic mode parameters of whitlockite were calculated. Some amounts of OH^--bearing whitlockite may be preserved and could be discovered in meteorites if whitlockite undergoes a low temperature process.

Keywords: Whitlockite; $Ca_9Mg(PO_3OH)(PO_4)_6$; High-pressure; High-temperature; Compressibility; Thermal expansion; Raman spectra; Dehydrogenation

1. Introduction

Whitlockite, $Ca_9Mg(PO_3OH)(PO_4)_6$, is one important natural calcium phosphate, commonly occurring in the terrestrial rocks (Lagier et al. 2003; Hughes et al. 2008; Adcock et al. 2014). $Ca_9Mg(PO_3OH)(PO_4)_6$ is the hydrogenated end member of the whitlockite-merrillite solid solution series (Adcock et al. 2017), with merrillite [$Ca_9NaMg(PO_4)_7$] being the anhydrous end-member (Xie et al. 2015). Merrillite is an accessory mineral found in many meteorites and it is a major carrier of rare earth elements, whereas whitlockite has not been confirmed in any type of meteorites (Adcock et al. 2017). Recently, natural merrillite was found as an inclusion in lower-mantle diamonds from the Rio Soriso area, Brazil (Kaminsky and Zedgenizov 2022). Previous studies indicated that whitlockite can transform into merrillite by heating at 1323 K (Hughes et al. 2008) or shock-compression (Adcock et al. 2017).

Whitlockite crystallizes in the trigonal system with the space group of *R3c* (Gopal et al. 1974). It consists of structural unit $[Mg(PO_4)_6]^{16-}$ and interstitial complex $[Ca_9(PO_3)(OH)]^{16+}$ (Xie et al. 2002; Hughes et al. 2006). The structural unit yields a “bracelet-and-pinwheel” arrangement (Moore 1973), which is composed of Mg octahedra decorated by six PO_4 tetrahedra in two kinds, as shown in Figure 1.

Some previous studies investigated the stability of whitlockite at high temperatures (Gopal et al. 1972; Hughes et al. 2006; Adcock et al. 2017). Gopal (1972) heated the natural whitlockite at 1200 °C overnight and refined the atomic arrangement to examine the structural relationships of $Ca_9Mg(PO_3OH)(PO_4)_6$ and β-$Ca_3(PO_4)_2$. Hughes et al. (2008) heated whitlockite at 773 K and 1323 K for 24 hours. Their results showed that whitlockite is stable at 773 K and dehydrogenates into merrillite at 1323 K. Adcock et al. (2017) showed whitlockite transforms into merrillite by shock-compression at conditions relevant to meteorites, which indicated that meteoritic merrillite may originally be formed from H^+-bearing whitlockite.

However, the physical properties of whitlockite at high pressures and high temperatures have been rarely investigated. The temperature for the dehydrogenation of whitlockite has not been well constrained since no continuous observation for the dehydrogenation at various temperatures is available. In the present study, the compressibility, thermal expansion, and the effect of pressure and temperature on the Raman active modes of whitlockite [$Ca_9Mg(PO_3OH)(PO_4)_6$] have been systematically investigated at high pressures up to ~ 15 GPa and high temperatures up to 1273 K by using in-situ X-ray diffraction and Raman spectroscopic measurements, respectively. In particular, the temperature-induced dehydrogenation of whitlockite into merrillite was observed in-situ.

2. Methods

2.1 Sample synthesis

By using pure reagents of $Mg(NO_3)\cdot 6H_2O$, CaO and H_3PO_4, high-purity whitlockite was obtained through a hydrothermal synthesis method. The method and procedure were similar to a previous study (Li et al. 2017). Firstly, according to the molality concentration of (Ca+Mg) of 0.1mol/L and molar ratio of Mg/(Ca+Mg) of 0.3, CaO and $Mg(NO_3)\cdot 6H_2O$ were added to deionized water to form a suspension. Secondly, H_3PO_4 was mixed with deionized water at desired concentration at a molar ratio of P/(Ca+Mg) of 1.67, stirring while pouring the solution into the suspension. Thirdly, HNO_3 was added to the mixture, and then the mixture was allowed to rest for a period of time until the precipitate dissolved. After the mixture was clarified, acetamide was added as the precipitation agent. The mixture was then enclosed into the autoclave and heated at 453 K for 6 hours. Finally, after natural cooling, the precipitation was washed, filtered, and dried at 333 K. The synthesized sample was characterized and confirmed as a single phase by powder X-ray diffraction method.

2.2 High- pressure X-ray diffraction and Raman spectra

The in-situ high-pressure X-ray diffraction measurements were carried out at the BL15U1 beamline in Shanghai Synchrotron Radiation Facility (SSRF) (Zhang et al. 2015). A symmetric piston cylinder diamond anvil cell (DAC) with 300-μm culets was adopted. The central part of a Re gasket was pre-intended to a thickness of 45 μm in which a cylindrical hole of 180 μm in diameter was drilled as the sample chamber. Small pieces of sample and gold were loaded into the chamber. A mixture of 4:1 deuterated methanol–ethanol was loaded as the pressure medium. The experimental pressures were calculated based on the equation of state (*EoS*) of gold given by Fei et al. (2007). Monochromatic X-ray with a wavelength of 0.6199 Å and a beam size of 2 μm (width) × 3 μm (height) was used in all the experiments. 2D images were recorded by a MAR-165 charge-couple device detector and integrated using the Dioptas program (Prescher and Prakapenka, 2015) to obtain one-dimensioned diffraction patterns. The sample-to-detector distance and the geometrical parameters of the detector were calibrated with cerium dioxide (CeO_2). All obtained X-ray diffraction patterns were analyzed by GSAS software package (Larson at al. 2004) to determine the unit-cell parameters and volume.

High-pressure Raman spectroscopic measurements were conducted with a symmetric piston cylinder DAC with 400-μm culets. The central part of T301 stainless steel gasket was pre-intended to a thickness of 70 μm in which a cylindrical hole of 240 μm in diameter was drilled as the sample chamber. Argon was used as pressure medium. A small piece of sample was loaded into the sample chamber with a ruby sphere as the pressure marker. Pressures were determined by the ruby fluorescence method (Mao et al. 1986). Raman spectra of whitlockite at different pressures and room temperature were recorded by a Horiba LabRam HR Evolution micro-Raman spectrometer with an 1800 lines/mm grating. A YAG: Nd^{3+} laser with a wavelength of 532 nm was used as an exciting source. The accumulation time of each spectrum was 60 s and the final spectrum at each pressure was the average of three measurements. The obtained Raman spectra were analyzed by using the PeakFit program (SPSS Inc., Chicago).

2.3 High-temperature X-ray diffraction and Raman spectra

In-situ synchrotron angle dispersive X-ray diffraction patterns at different temperatures were collected at the beamline BL14B1 of SSRF (Yang et al. 2015). A powdered sample was loaded into a fused quartz capillary, which was heated in a custom-made furnace to reach the target temperature in a speed of 30 K/min. The temperature was measured by a K-type thermocouple and controlled with an accuracy of about ± 1 K. A monochromatic X-ray beam with a wavelength of 0.6886 Å and a beam size of 180 μm (width) × 200 μm (height) was used. The Mythen 1K linear detector was adopted to collect the data in transmission mode (Gao et al. 2016). The wavelength of the X-ray was calibrated by LaB_6 standard from NIST (660b). The sample was kept at a desired temperature about 5 mins for thermal equilibration before each measurement. One-dimensional X-ray diffraction patterns were collected in the 2θ range of 5~30° with a step of 0.01°. All collected X-ray diffraction patterns were analyzed by GSAS software package (Larson and Von Dreele 2004) to obtain the unit-cell parameters and volume.

The Raman spectra of synthetic whitlockite at various temperatures and ambient pressure were collected using a Horiba LabRam HR Evolution micro-Raman spectrometer with an 1800 gr/mm grating. A YAG: Nd^{3+} laser with a wavelength of 532 nm and a power of 20 mW was adopted. The Raman spectrometer was calibrated with a single crystal of silicon to the peak at 520 cm^{-1}. Polycrystalline whitlockite of approximate 100 × 100 × 60 μm in size was placed on sapphire window which was put into an alumina chamber in Linkam TS 1500, and the experiment was performed up to 1173 K by using a heating stage consisting of an electric-resistance heater with a water-cooling system which was used to prevent damages to the optical system and the sample stage. The temperature was measured by an S-type thermocouple and controlled by a program. The sample was hold at each temperature for about 10 min for thermal equilibrium. The accumulation time for each collection was 60 s, and the final spectrum at each temperature was the average of three measurements. The Raman spectra were analyzed by the PeakFit program (SPSS Inc., Chicago).

3. Result and discussion

3.1 High-pressure in situ X-ray diffraction

Figure 2 displays the typical X-ray diffraction patterns of whitlockite at different pressures, where all the peaks shift to higher 2θ region with increasing pressure. No pressure-induced phase transition is observed. The unit-cell parameters and volume of whitlockite at ambient conditions are a = 10.357(1) Å, c = 37.119(5) Å, V = 3448.0(6) $Å^3$, which are consistent with previous results of Gopal (1974).

The refined unit-cell parameters and volume of whitlockite are listed in Table 1. The relative changes of the unit-cell parameters and volume with pressures for whitlockite are plotted in Figure 3, with a following third-order Birch-Murnaghan *EoS*

(Birch 1947) fitting to obtain the elastic parameters:

$$P = \frac{3K_0}{2}\left[\left(\frac{V_0}{V}\right)^{\frac{7}{3}} - \left(\frac{V_0}{V}\right)^{\frac{5}{3}}\right]\left\{1+\frac{3}{4}\left(K_0' - 4\right)\left[\left(\frac{V_0}{V}\right)^{\frac{2}{3}} - 1\right]\right\} \quad (1)$$

where P, V, V_0, K_0, and K_0' are pressure, volume, zero-pressure volume, isothermal bulk modulus and its pressure derivative, respectively. The least-squares fitting was performed by using *EoSFit* program (Angel 2000), giving V_0 = 3459.1(56) Å^3, K_0 = 79(4) GPa, K_0' = 4.3(6). When K_0' was fixed at 4, a second-order Birch-Murnaghan *EoS*, the fitting yields K_0 = 81(1) GPa. The V_0 = 3459.1 Å^3 obtained by fitting was used for normalization shown in Figure 3. The obtained bulk modulus is comparable to some other phosphates, as listed in Table 2. It is noted that different crystal structure and chemical composition have effects on the bulk modulus of phosphates. In trigonal structure with a space group of *R3c*, three kinds of PO_4 tetrahedra with averaged P-O bond lengths of 1.540, 1.561 and 1.538 Å exist in $Ca_9Mg(PO_4)_7(OH)$, $Ca_9NaMg(PO_4)_7$ and β-$Ca_3(PO_4)_2$, respectively, at ambient conditions (Gopal et al. 1974; Moore 1973; Yashima et al. 2003). Three kinds of CaO_8 and one MgO_6 polyhedra present in $Ca_9Mg(PO_4)_7(OH)$. Two kinds of CaO_8, one CaO_9, one NaO_6 and one MgO_6 polyhedra present in $Ca_9NaMg(PO_4)_7$. Two kinds of CaO_8, one CaO_7, one CaO_3 and one CaO_6 polyhedra present in β-$Ca_3(PO_4)_2$. In trigonal structure with a space group of *R-3m*, one kind of PO_4 tetrahedron with averaged P-O bond lengths of 1.533, 1.553 and 1.549 Å exists in γ-$Ca_3(PO_4)_2$, $Sr_3(PO_4)_2$, and $Pb_3(PO_4)_2$, respectively, at ambient conditions (Sugiyama and Tokonami 1987; Qin et al. 2014). Two kinds of metal-oxygen polyhedra with coordination of 12 and 10 present in γ-$Ca_3(PO_4)_2$, $Sr_3(PO_4)_2$ and $Pb_3(PO_4)_2$ with different metal-oxygen bond lengths due to different cations. In hexahonal apatites with a space group of $P6_3/m$, one PO_4 tetrahedron, one CaO_9 and one CaO_6X (X = F, Cl, OH) polyhedra exist (Hughes et al. 1989). In monoclinic apatites with a space group of *$P2_1/b$*, three kinds of PO_4 tetrahedra, three kinds of CaO_9 and two kinds of CaO_6X (X = Cl, OH) polyhedra exist (Suetsugu et al. 2001).

In order to obtain the axial compressibility of whitlockite, simply by substituting the cube of the lattice parameter (a^3 or c^3) for the volume, the values of a^3 and c^3 were fitted by a ‘‘linearized’’ third-order Birch-Murnaghan *EoS* and following the procedure implemented in the *EoSFit* program (Angel 2000). The refined initial incompressible parameters (that is 1/3 of the axial incompressibilities; see Angel (2000)) are K_a = 82.5(15) GPa and K_c = 77.0(14) GPa when K_0' fixed at 4, which indicates that whitlockite has an axial elastic anisotropy since the *c*-axis is more compressible than the *a*-axis based on the bracelet-and-pinwheel structure (Figure 1).

3.2 High-pressure Raman spectra

As mentioned above, whitlockite has a trigonal structure belonging to the space group *R3c*. The Raman active modes of whitlockite can be predicted by symmetry-adapted modes (Kroumova et al. 2003) as following:

$$\Gamma = 44A_1 + 89E \qquad (2)$$

where A_1, E and Γ represent non-degenerate, double-degenerate, and the total irreducible Raman vibrations, respectively. Thus, a total of 133 Raman active modes are predicated. However, due to some undetected weak Raman active modes and/or overlapping, the numbers of observed Raman bands are fewer than the theoretically predicted. The Raman spectrum of whitlockite at ambient conditions is consistent with previous studies (Jolliff et al. 1996; 2006), and some Raman modes can be distinguished (Figure 4). In the high frequency range (above 900 cm^{-1}), the spectrum contains peaks at 989, 971 and 961 cm^{-1} for the ν_1 symmetric stretching vibrations of

P-O bonds in PO_4 tetrahedron. The peak at 920 cm^{-1} is assigned to the v_1 symmetric stretching vibration of the HPO_4^{2-} group. Moreover, the peaks at 1093, 1064 and 1025 cm^{-1} are assigned to v_3 anti-symmetric stretching vibrations of the P-O bonds in PO_4 tetrahedron. In the middle frequency range (350-700 cm^{-1}), the peaks at 486, 460, 430 and 405 cm^{-1} are assigned to the v_2 bending vibrations of the O-P-O bonds in PO_4 tetrahedron, and the peaks at 625, 604 and 560cm^{-1} are assigned to the v_4 bending vibrations of the O-P-O bonds in PO_4 tetrahedron. In the low frequency range (below 350 cm^{-1}), the peaks at 280 and 160 cm^{-1} are the external modes.

The Raman spectra of whitlockite were collected to 15.3 GPa and the representative spectra at various pressures were also showed in Figure 4. It is noted that no new peaks appear during compression, which indicates that whitlockite does not exhibit any pressure-induced phase transition. This is consistent with the observation of high-pressure X-ray diffraction measurements. Figure 5 shows the changes of Raman shifts for different modes with pressure. It is clear that all the peaks systematically shift to higher frequency with different slope with increasing pressure. The correlations between Raman shift of different modes and pressure fitted by linear regressions are listed in Table 3. The pressure dependence of anti-symmetric and symmetric stretching modes (v_3 and v_1) (3.40 ~ 5.25 cm^{-1}/GPa) are larger than those of the bending modes (v_4 and v_2) and the external modes (1.38 ~ 2.88 cm^{-1}/GPa) excluding the band at 430 cm^{-1}, indicating that the stretching vibrations in high frequency range are more sensitive to pressure than the bending vibrations and the external modes in the low frequency range.

The isothermal bulk modulus and pressure-dependence of Raman vibrations can be used to obtain the isothermal mode Grüneisen parameters γ_{iT}, defined by the following equation (Grüneisen 1912):

$$\gamma_{iT} = \frac{\left(\frac{\delta v_i}{\delta P}\right) K_0}{v_i} \tag{3}$$

where v_i, P, and K_0 are the frequency of the i^{th} mode, the pressure and the isothermal bulk modulus, respectively. The isothermal bulk modulus $K_0 = 79$ GPa obtained in this study was used. The values of γ_{iT} for different modes of whitlockite are also listed in Table 3.

The average value for the mode Grüneisen parameters (Table 3) of the bands associated to phosphate group vibrations is 0.38, which is larger than that of merrillite and smaller than that of fluorapatite. PO_4^{3-} groups exist in whitlockite, merrillite and fluorapatite with different geometrical arrangement. This difference may be caused by different crystal structure and other components (such as halogens and/or OH) excluding phosphorus oxygen tetrahedron. On the other hand, the average value for the lattice modes is 0.44, which is larger than the average of the internal PO_4 modes, illustrating the lattice modes largely affect the isothermal mode Grüneisen parameters. The pressure dependence of the Raman mode frequency is affected by the "stiffness" of the local interatomic interactions in the structural unit that most directly contributes to that vibrational mode. Therefore, the different Grüneisen parameters might be due to the result that calcium/magnesium polyhedron is more compressible (flexible) than the phosphate tetrahedral (Comodi et al. 2001; Pankrushina et al. 2022).

3.3 High-temperature in situ X-ray diffraction

Figure 6 illustrates the typical X-ray diffraction patterns of $Ca_9Mg(PO_3OH)(PO_4)_6$ up to 1223 K. It is clear that the X-ray diffraction peaks shift to the lower 2θ region with increasing temperature. At 1073 K new peaks appear at 2θ = 12.97° and 13.54° and become stronger with further heating (Figure 6b). At 1173 K several other new peaks appear at 2θ = 9.57°, 12.64°, 13.05, 13.93°, 14.03° and 14.20°

(Figure 6b). Additionally, the split peaks at $2\theta = 14.58°$ become one peak at 1223 K. Hughes et al. (2008) heated whitlockite at 773 K and 1323 K for 24 hours and found that whitlockite is stable at 773 K and completely dehydrogenates into merrillite at 1323 K. They only heated the sample at two temperatures and didn't constrain the dehydrogenated temperature. These new peaks we observe indicate some part of whitlockite undergoes a temperature-induced dehydrogenation above 973 K. Therefore, it is reasonable to infer that whitlockite dehydrogenates to merrillite in the present study. The refined unit-cell parameters and volume for whitlockite at different temperatures before dehydrogenation are listed in Table 4.

The relative variations of unit-cell parameters and volume of whitlockite at different temperatures up to 973 K are plotted in Figure 7. The thermal expansion coefficient of whitlockite can be obtained by the following expression (Fei 1995):

$$\ln (V / V_0) = \alpha_V (T - T_0) \tag{4}$$

Similarly, the axial thermal expansion coefficients can also be obtained as follows:

$$\ln (a / a_0) = \alpha_a (T - T_0) \tag{5}$$

$$\ln (c / c_0) = \alpha_c (T - T_0) \tag{6}$$

The calculated thermal expansion coefficients are listed in Table 5. The thermal expansion coefficients of whitlockite were obtained as $4.05(8) \times 10^{-5}$ K^{-1}, $1.07(5) \times 10^{-5}$ K^{-1}, and $1.91(6) \times 10^{-5}$ K^{-1} for volume, *a*- and *c*-axis, respectively. The axial thermal expansion along the *a*-axis is 44% smaller than that along the *c*-axis, indicating an axial anisotropic thermal expansion.

Whitlockite anisotropic axial thermal expansivity and compressibility can be explained by the "path" of the structure (Cameron et al. 1973). As mentioned above, the structural units have a "bracelet-and-pinwheel" arrangement (Figure 1), and the path along *a*-axis crosses the structural unit with larger atom density and tighter arrangement, but the path parallel to the *c*-axis does not (Hughes et al. 2008).

For comparison, the thermal expansion coefficients of other phosphate minerals are also listed in Table 5. The thermal expansion coefficient of whitlockite is smaller than that of merrillite (Jia et al. 2020b), and larger than those of hydroxyapatite (Hovis et al. 2014), β-$Ca_3(PO_4)_2$ (Zhai et al. 2014), tuite (Zhai et al. 2011a), fluorapatite (Chernorukov et al. 2011; Hovis et al. 2015) and chlorapatite (Hovis et al. 2015), which might be attributed to different chemical composition, crystal structure, crystallinity, and bond strength. Different chemical composition is important - for example, the different proportions of F, Cl, OH (and amount of vacancies) in apatite is an important factor, because halogens in binary and ternary apatites are difficult to accommodate in solid solution. An additional off-mirror F site appears in F-Cl-apatites (OH-free) (Hughes et al. 2014). The chemical composition of β-$Ca_3(PO_4)_2$ and tuite is same, but the crystal structure and bond strength are different, resulting in different thermal expansion coefficient. Therefore, it is difficult to conclude which factor is the most important to influence the thermal expansion coefficient.

3.4 High-temperature Raman spectra

The typical Raman spectra at various temperatures are plotted in Figure 8, where all the Raman bands become broader and shift to lower frequency regions with increasing temperature. It is noted that the peak at 920 cm^{-1} attributed to the ν_1 symmetric stretching vibrations of HPO_4^{2-} becomes weak with increasing temperature and disappears at 1023 K. This phenomenon is consistent with the results of high-temperature X-ray diffraction measurements, indicating a temperature-induced dehydrogenation of whitlockite. After cooling to 298 K, the temperature-induced dehydrogenated product does not transform back into its initial structure, which means an irreversible reaction. In previous studies (Hughes et al. 2006; Adcock et al. 2017), by the analysis of the crystal structure and the obtained from whitlockite at high temperature, it has been demonstrated that merrillite is the dehydrogenated product of whitlockite.

Figure 9 displays the variations of Raman shift for different modes with temperature. All Raman modes shift linearly and continuously. The relationships between vibration mode *v* and temperature T fitted by linear regressions are listed in Table 3. The range of temperature dependence for whitlockite is from -0.049 to -0.006cm^{-1}/K. The temperature dependences of anti-symmetric stretching modes and symmetric stretching modes (v_3 and v_1) are -0.045~- 0.015 cm^{-1}/K, whereas those of bending modes (v_4 and v_2) are -0.017~ -0.006 cm^{-1}/K. Thus, the effect of temperature on v_3 and v_1 modes is stronger than that on v_4 and v_2 bending modes.

For the internal PO_4 vibrations of whitlockite, the symmetric stretching modes are more susceptible to temperature and pressure than the bending modes. It might be attributed to the stretching modes of PO_4 with less spatial hindrance to move easily as temperature and pressure increase, whereas bending modes of PO_4 may encounter more spatial hindrance because they vibrate in directions with more repulsion.

Based on the thermal expansion coefficient and the temperature dependence of active Raman modes, the isobaric mode Grüneisen parameter γ_{iP} can be obtained by the following equation (Gillet et al. 1989; Okada et al. 2008):

$$\gamma_{iP} = - 1/ \alpha\ (\partial \ln \nu_i / \partial T)_P \qquad (7)$$

where v_i and α are the frequency of the *i*th mode and the thermal expansion coefficient, respectively. The obtained thermal expansion coefficient of 4.05×10^{-5} K^{-1} for whitlockite in this study was adopted. The calculated values of γ_{iP} are also listed in

Table 3, in the range of 0.37~4.25. In fact, the values of isobaric mode Grüneisen parameters of the internal PO_4 modes are smaller than those of the lattice modes. This phenomenon might be due to differences in coordination numbers and charges (Gillet et al. 1989). For the internal PO_4 modes, low coordination (four for P) and higher charged atoms lead to small γ_{iP}. For the lattice modes, lower charged atoms, and higher coordination account for large γ_{iP} (Gillet et al. 1989). Such behavior is not only observed in whitlockite, but also found in some other minerals for which high-temperature data are available, including merrillite (Jia et al. 2020b), Mg_2SiO_4 (Dietrich and Arndt 1982), pyrope and andradite (Gillet et al. 1992).

3.5 Intrinsic anharmonicity

Based on the obtained results, the intrinsic anharmonicity of whitlockite can be calculated. As shown in Table 3, the values of isothermal mode Grüneisen parameters and those of isobaric mode Grüneisen parameters for the same vibrations are not equal. Therefore, an intrinsic anharmonicity exists. The intrinsic anharmonic mode parameter β_i, can be estimated using the values of Grüneisen parameters γ_{iP} and γ_{iT} as follows (Mammone et al. 1979):

$$\beta_i=\left(\frac{\partial \ln \nu_i}{\partial T}\right)_V=\alpha\,(\gamma_{iT}-\gamma_{iP})_T \tag{8}$$

The calculated values of β_i for different vibrational modes are also list in Table 3, ranging from -15.80×10^{-5} K^{-1} to 0.69×10^{-5} K^{-1} with an average intrinsic anharmonic mode parameter for PO_4 of -1.01×10^{-5} K^{-1}. The absolute average intrinsic anharmonic mode parameter of whitlockite is higher than that of tuite (-0.80×10^{-5} K^{-1}) (Zhai et al. 2011a) and merrillite (0.98×10^{-5} K^{-1}) (Jia et al. 2020a). Compared with SiO_4 vibrations in silicate minerals such as grossular (-1.75×10^{-5} K^{-1}) (Gillet et al. 1992), the PO_4 vibrations in whitlockite show lower absolute average intrinsic anharmonic mode parameter.

The data of X-ray diffraction and Raman spectra under high temperature indicate that a temperature-induced dehydrogenation of whitlockite forms anhydrous end-member merrillite. Combined with previous study by Hughes et al. (2008), the atomic arrangement of the whitlockite is changed by heating and the charge-balancing substitution between whitlockite and merrillite is H↔$Ca_{0.5}$. The whitlockite-merrillite solid solution series differ due to the temperature and content of hydrogen.

4. Implication

Previous studies on Martian and lunar meteorites suggest they contain water. Detectable amounts of OH in Martian and lunar apatite were found in previous studies (Watson et al. 1994; Leshin 2000; Boyce et al. 2010; McCubbin et al. 2010; Greenwood et al. 2011; Liu et al. 2012; Gross et al. 2013; Smith et al. 2020). Merrillite was also found in Martian and lunar meteorites, as well as in carbonaceous chondrites (Martinez 2021; Martinez and Brearley 2022), while whitlockite has not been confirmed in any type of meteorite (Adcock et al. 2017). According to this study, the dehydrogenation of whitlockite begins above 973 K at ambient pressure. Though there is no information about the effect of pressure on the dehydrogenation of whitlockite, it is reasonable to deduce that some meteoritic merrillites may be produced by OH^--bearing whitlockite due to some kinds of high-temperature processes. If the temperature of such process is not so high, some part of OH^--bearing whitlockite may remain and could be distinguished in meteorites.

Acknowledgements

The authors thanks Dr. Speziale for his editorial handling and helpful comments and suggestion, and also appreciate Dr. Marina Martinez and Prof. Mario Tribaudino for their critical comments and suggestion. This work was financially supported by the Strategic Priority Research Program of Chinese Academy of Sciences (Grant No. XDB41000000), the National Natural Science Foundation of China (Grant No. 42120104005), the International Partnership Program of Chinese Academy of Sciences (Grant No. 132852KYSB20200011), Guizhou Provincial 2021 Science and Technology Subsidies (No. GZ2021SIG). The in-situ synchrotron X-ray diffraction measurements were carried out at the BL15U1 and BL14B1 beamlines of the Shanghai Synchrotron Radiation Facility (Proposal Nos. 2018-SSRF-PT-007075 and 2020-SSRF-PT-012550).

References

Adcock, C.T., Hausrath, E.M., Forster, P.M., Tschauner, O., and Sefein, K.J. (2014) Synthesis and characterization of the Mars-relevant phosphate minerals Fe- and Mg-whitlockite and merrillite and a possible mechanism that maintains charge balance during whitlockite to merrillite transformation. American Mineralogist, 99, 1221-1232.

Adcock, C.T., Tschauner, O., Hausrath, E.M., Udry, A., Luo, S.N., Cai, Y., Ren, M., Lanzirotti, A., Newville, M., Kunz, M., and Lin, C. (2017) Shock-transformation of whitlockite to merrillite and the implications for meteoritic phosphate. Nature Communications, 8, 1-8.

Angel, R.J. (2000) Equations of state. Reviews in Mineralogy and Geochemistry, 41, 35-59.

Birch, F. (1947) Finite elastic strain of cubic crystals. Physical Review, 71, 809-824.

Boyce, J.W., Liu, Y., Rossman, G.R., Guan, Y., Eiler, J.M., Stolper, E.M., and Taylor, L.A. (2010) Lunar apatite with terrestrial volatile abundances. Nature, 466, 466-469.

Brunet, F., Allan, D.R., Redfern, S.A.T., Angel, R.J., Miletich, R., Reichmann, H.J., Sergent, J., and Hanfland, M. (1999) Compressibility and thermal expansivity of synthetic apatites, $Ca_5(PO_4)_3X$ with X = OH, F and Cl. European Journal of Mineralogy, 11, 1023-1035.

Cameron, M., Sueno, S., Prewitt, C.T., and Papike, J.J. (1973) High-temperature crystal chemistry of acmite, diopside, hedenbergite, jadeite, spodumene, and ureyite. American Mineralogist, 58, 594-618.

Chernorukov, N.G., Knyazev, A.V., and Bulanov, E.N. (2011) Phase transitions and thermal expansion of apatite-structured compounds. Inorganic Materials, 47, 172-177.

Comodi, P., Liu, Y., Zanazzi, P.F., and Montagnoli, M. (2001) Structural and vibrational behaviour of fluorapatite with pressure. Part I: in situ single-crystal X-ray diffraction investigation. Physics and Chemistry of Minerals, 28, 219-224.

Dietrich, P., and Arndt, J. (1982) Effects of pressure and temperature on the physical behavior of mantle-relevant olivine, orthopyroxene and garnet. II infrared absorption and microscopic grueneisen parameters. In: High Pressure Researches in Geoscience, p. 307-319, E. Schweizerbart'sche Verlagsbuchhandlung, Stuttgart.

Fei, Y. (1995) Thermal expansion. In T.J. Ahrens, Eds., Mineral Physics and Crystallography: A Handbook of Physical Constants, p. 29-44, American Geophysical Union, Washington DC.

Frondel, C. (1941) Whitlockite a new calcium phosphate, $Ca_3(PO_4)_2$. American Mineralogist, 26, 145-152.

Gao, M., Gu, Y., Gong, Z., Li, L., Gao, X., and Wen, W. (2016) Facile usage of a MYTHEN 1K with a Huber 5021 diffractometer and angular calibration in *operando* experiments. Journal of Applied Crystallography, 49, 1182-1189.

Gillet, P., Fiquetw, G., Malézieux, J.M., and Geiger, C.A. (1992) High-pressure and high-temperature Raman spectroscopy of end-member garnets: pyrope, grossular and andradite. European Journal of Mineralogy, 4, 651-664.

Gillet, P., Guyot, F., and Malézieux, J.M. (1989) High-pressure, high-temperature Raman spectroscopy of Ca_2GeO_4 (olivine form): some insights on anharmonicity. Physics of the Earth and Planetary Interiors, 58, 141-154.

Gopal, R., and Calvo, C. (1972) Structural relationship of whitlockite and β-$Ca_3(PO_4)_2$. Nature Physical Science, 237, 30-32.

Gopal, R., Calvo, C., Ito, J., and Sabine, W.K. (1974) Crystal structure of synthetic Mg-whitlockite, $Ca_{18}Mg_2H_2(PO_4)_{14}$. Canadian Journal of Chemistry, 52, 1155-1164.

Greenwood, J.P., Itoh, S., Sakamoto, N., Warren, P., Taylor, L., and Yurimoto, H. (2011) Hydrogen isotope ratios in lunar rocks indicate delivery of cometary water to the Moon. Nature Geoscience, 4, 79-82.

Gross, J., Filiberto, J., and Bell, A.S. (2013) Water in the martian interior: Evidence for terrestrial MORB mantle-like volatile contents from hydroxyl-rich apatite in olivine–phyric shergottite NWA 6234. Earth and Planetary Science Letters, 369, 120-128.

Grüneisen, E. (1912) Theorie des festen Zustandes einatomiger Elemente. Annalen der Physik, 344, 257-306.

Hovis, G., Abraham, T., Hudacek, W., Wildermuth, S., Scott, B., Altomare, C., Medford, A., Conlon, M., Morris, M., Leaman, A., Almer, C., Tomaino, G., and

Harlov, D. (2015) Thermal expansion of F-Cl apatite crystalline solutions. American Mineralogist, 100, 1040-1046.

Hovis, G., Scott, B., Altomare, C., Leaman, A., Morris, M., Tomaino, G., and McCubbin, F. (2014) Thermal expansion of fluorapatite-hydroxylapatite crystalline solutions. American Mineralogist, 99, 2171-2175.

Hughes, J.M., Cameron, M., and Crowley, K.D. (1989) Structural variations in natural F, OH, and Cl apatites. American Mineralogist, 74, 870-876.

Hughes, J.M., Jolliff, B.L., and Gunter, M.E. (2006) The atomic arrangement of merrillite from the Fra Mauro Formation, Apollo 14 lunar mission: The first structure of merrillite from the Moon. American Mineralogist, 91, 1547-1552.

Hughes, J.M., Jolliff, B.L., and Rakovan, J. (2008) The crystal chemistry of whitlockite and merrillite and the dehydrogenation of whitlockite to merrillite. American Mineralogist, 93, 1300-1305.

Hughes, J.M., Nekvasil, H., Ustunisik, G., Lindsley, D. H., Coraor, A. E., Vaughn, J., Phillips, B.L., McCubbin, F.M., and Woerner, W. R. (2014) Solid solution in the fluorapatite-chlorapatite binary system: High-precision crystal structure refinements of synthetic F-Cl apatite. American Mineralogist, 99, 369-376.

Jia, M., Hu, X., Liu, Y, Jiang, S., Wu, X., and Zhai S. (2020a) X-ray diffraction and Raman spectra of merrillite at high pressures. High Pressure Research, 40, 411-422.

Jia, M., Zhai, K., Gao, M., Wen, W., Liu, Y., Wu, X., and Zhai, S. (2020b) Raman spectra and X-ray diffraction of merrillite at various temperatures. Vibrational Spectroscopy, 106, 103005.

Jolliff, B.L., Hughes, J.M., Freeman, J.J., and Zeigler, R.A. (2006) Crystal chemistry of lunar merrillite and comparison to other meteoritic and planetary suites of whitlockite and merrillite. American Mineralogist, 91, 1583-1595.

Kaminsky, F.V., and Zedgenizov, D.A. (2022) First find of merrillite, $Ca_3(PO_4)_2$, in a terrestrial environment as an inclusion in lower-mantle diamond. American Mineralogist, 107, 1652-1655.

Kroumova, E., Aroyo, M.I., Perez-Mato, J.M., Kirov, A., Capillas, C., Ivantchev, S., and Wondratschek, H. (2003) Bilbao crystallographic server: Useful databases and tools for phase-transition studies. Phase Transitions, 76, 155-170.

Lagier, R., and Baud, C.A. (2003) Magnesium whitlockite, a calcium phosphate crystal of special interest in pathology. Pathology - Research and Practice, 199, 329-335.

Larson, A.C., and Von Dreele, R.B. (2004) General Structure Analysis System (GSAS). Los Alamos National Laboratory Report LAUR, p. 86-748.

Leshin, L.A. (2000) Insights into martian water reservoirs from analyses of martian meteorite QUE94201. Geophysical Research Letters, 27, 2017-2020.

Li, G., Wang, P., and Liu, C. (2017) Hydrothermal synthesis of whitlockite. Journal of Inorganic Materials, 32, 1128-1132.

Liu, Y., Guan, Y., Zhang, Y., Rossman, G.R., Eiler, J.M., and Taylor, L.A. (2012) Direct measurement of hydroxyl in the lunar regolith and the origin of lunar surface water. Nature Geoscience, 5, 779-782.

Mammone, J.F., and Sharma, S.K. (1979) Pressure and temperature dependence of the Raman spectra of rutile-structure oxides. Carnegie Institution of Washington Year Book, 78, 369-373.

Mao, H.K., Xu, J., and Bell, P.M. (1986) Calibration of the ruby pressure gauge to 800 kbar under quasi-hydrostatic conditions. Journal of Geophysical Research: Solid Earth 91, 4673-4676.

Martinez, M. (2021). Microstructural and microchemical studies of fluid-chondrule interactions in a pristine CR carbonaceous chondrite and apatite in Martian Nakhlites. Doctoral dissertation, The University of New Mexico.

Martinez, M., and Brearley, A.J. (2022) Smooth rims in Queen Alexandra Range (QUE) 99177: Fluid-chondrule interactions and clues on the geochemical conditions of the primordial fluid that altered CR carbonaceous chondrites. Geochimica et Cosmochimica Acta, 325, 39-64

Matsukage, K.N., Ono, S., Kawamoto, T., and Kikegawa, T. (2004) The compressibility of a natural apatite. Physics and Chemistry of Minerals, 31, 580-584.

McCubbin, F.M., Steele, A., Nekvasil, H., Schnieders, A., Rose, T., Fries, M., Carpenter, P.K., and Jolliff, B.L. (2010) Detection of structurally bound hydroxyl in fluorapatite from Apollo Mare basalt 15058, 128 using TOF-SIMS. American Mineralogist, 95, 1141-1150.

Moore, P.B. (1973) Bracelets and pinwheels: A topological-geometrical approach to the calcium orthosilicate and alkali sulfate structures. American Mineralogist, 58, 32-42.

Okada, T., Narita, T., Nagai, T., and Yamanaka, T. (2008) Comparative Raman spectroscopic study on ilmenite-type $MgSiO_3$ (akimotoite), $MgGeO_3$, and $MgTiO_3$ (geikielite) at high temperatures and high pressures. American Mineralogist, 93, 39-47.

Pankrushina, E.A., Shchapova, Y.V., and Votyakov, S.L. (2022) Thermal behavior and anharmonicity of PO_4-tetrahedral vibrations in natural fluorapatite by polarized Raman spectroscopy. Journal of Raman Spectroscopy, 53, 832-845.

Prescher, C., and Prakapenka, V.B. (2015) Dioptas: a program for reduction of two-dimensional x-ray diffraction data and data exploration. High Pressure Research, 35, 223-230.

Qin, F., Wu, X., Zhai, S., Qin, S., Yang, K., Chen, D., and Li, Y. (2014) Pressure-induced phase transition of lead phosphate $Pb_3(PO_4)_2$: X-ray diffraction and XANES. Phase Transitions, 87, 1255-1264.

Smith, A., Hallis, L.J., Nagashima, K., and Huss, G.R. (2020) Volatile abundances and hydrogen isotope ratios of apatite in Martian basaltic breccia NWA 11522—A paired stone of NWA 7034. Meteoritics & Planetary Science, 55, 2587-2598.

Suetsugu, Y., Ikoma, T., and Tanaka, J. (2001) Single crystal growth and structure analysis of monoclinic hydroxyapatite. Key Engineering Materials 192-195, 287-290.

Sugiyama, K., and Tokonami, M. (1987) Structure and crystal chemistry of a dense polymorph of tricalcium phosphate $Ca_3(PO_4)_2$: A host to accommodate large lithophile elements in the Earth’s mantle. Physics and Chemistry of Minerals, 15, 125-130.

Watson, L.L., Hutcheon, I.D., Epstein, S., and Stolper, E.M. (1994) Water on Mars: Clues from deuterium/hydrogen and water contents of hydrous phases in SNC meteorites. Science, 265, 86-90.

Xie, X., Minitti, M.E., Ming, C., Mao, H.K., Wang, D., Shu, J., and Fei, Y. (2002) Natural high-pressure polymorph of merrillite in the shock vein of the Suizhou meteorite. Geochimica et Cosmochimica Acta, 66, 2439-2444.

Xie, X., Yang, H., Gu, X., and Downs, R. T. (2015) Chemical composition and crystal structure of merrillite from the Suizhou meteorite. American Mineralogist, 100, 2753-2756.

Yang, T., Wen, W., Yin, G., Li, X., Gao, M., Gu, Y., Li, L., Liu, Y., Lin, H., Zhang, X., Zhao, B., Liu, T., Yang, Y., Li, Z., Zhou, X., and Gao, X. (2015) Introduction of the X-ray diffraction beamline of SSRF. Nuclear Science and Techniques, 26, 020101.

Yashima, M., Sakai, A., Kamiyama, T., and Hoshikawa, A. (2003) Crystal structure analysis of β-tricalcium phosphate $Ca_3(PO_4)_2$ by neutron powder diffraction. Journal of Solid State Chemistry, 17, 272-277.

Zhai, S., Akaogi, M., Kojitani, H., Xue, W., and Ito, E. (2014) Thermodynamic investigation on β- and γ-$Ca_3(PO_4)_2$ and the phase equilibria. Physics of the Earth and Planetary Interiors, 228, 144-149.

Zhai, S., Liu, X., Shieh, S.R., Zhang, L., and Ito, E. (2009) Equation of state of γ-tricalcium phosphate, γ-$Ca_3(PO_4)_2$, to lower mantle pressures. American Mineralogist, 94, 1388-1391.

Zhai, S., and Wu, X. (2010) X-ray diffraction study of β-$Ca_3(PO_4)_2$ at high pressure. Solid State Communications, 150, 443-445.

Zhai, S., Xue, W., Lin, C., Wu, X., and Ito, E. (2011a) Raman spectra and X-ray diffraction of tuite at various temperatures. Physics and Chemistry of Minerals, 38, 639-646.

Zhai, S., Xue, W., Yamazaki, D., Shan, S., Ito, E., Tomioka, N., Shimojuku, A., and Funakoshi, K. (2011b) Compressibility of strontium orthophosphate $Sr_3(PO_4)_2$ at high pressure. Physics and Chemistry of Minerals, 38, 357-361.

Zhang, L., Yan, S., Jiang, S., Yamg, K., Wang, H., He, S., Liang, D., Zhang, L., He, Y., Lan, X., Mao, C., Wang, J., Jiang, H., Zheng, Y., Dong, Z., Zeng, L., and Li, A. (2015) Hard X-ray micro-focusing beamline at SSRF. Nuclear Science and Techniques, 26, 060101.

Figure captions

Fig. 1 The arrangement of the bracelet-and-pinwheel structure units in whitlockite. A $[Mg(PO_4)_6]^{16-}$ structural unit is shown separately at the right corner

Fig. 2 Representative X-ray diffraction patterns of whitlockite up to 14.90 GPa at room temperature

Fig. 3 Relative changes of unit-cell parameters and volume of whitlockite at different pressures. The values of V_0 = 3459.1 Å^3, a_0 = 10.357 Å and c_0 = 37.119 Å were adopted for normalization

Fig. 4 Typical Raman spectra of whitlockite at different pressures and room temperature

Fig. 5 Pressure dependence of the Raman bands of whitlockite at room temperature, the solid, open and half-open symbols repesent the measured Raman shifts at different pressures, and the dot-dashed lines represent linear fittings. The error bar is the standard deviation

Fig. 6 Representative X-ray diffraction patterns of whitlockite up to 1223 K at ambient pressure in the 2 theta ranges of 5~25° (a) and 9~15° (b). The asterisk symbols indicate new XRD peaks. The XRD pattern labelled with 314 K was collected after cooling to room temperature

Fig. 7 Relative changes in unit-cell parameters and volume with temperature. The values of a_0 = 10.3564 Å, c_0 = 37.1247 Å and V_0 = 3448.3 Å^3 obtained from the XRD pattern collected at 306 K before heating were adopted for normalization

Fig. 8 Typical Raman spectra of whitlockite at different temperatures and ambient pressure. The spectrum labelled with 298 K* was collected after cooling to room temperature

Fig. 9 Temperature dependence of the Raman bands of whitlockite at ambient pressure

Table 1 Unit-cell parameters and volume of whitlockite at different pressures

P(GPa)	*a*(Å)	*c* (Å)	*V*(Å^3)
0.0001	10.357(1)	37.119(5)	3448.0(6)
1.12(1)	10.305(1)	37.117(7)	3413.5(8)
2.80(1)	10.264(1)	36.762(3)	3353.8(4)
3.47(1)	10.235(1)	36.647(5)	3324.5(6)
4.49(1)	10.199(1)	36.523(4)	3290.1(4)
4.92(1)	10.181(1)	36.464(4)	3273.5(5)
5.66(1)	10.156(1)	36.369(4)	3248.6(4)
6.96(1)	10.109(1)	36.234(5)	3206.6(6)
7.63(1)	10.098(1)	36.146(4)	3191.9(5)
8.54(1)	10.066(1)	36.093(5)	3166.9(5)
9.04(1)	10.047(1)	36.004(6)	3147.1(6)
9.56(1)	10.035(1)	35.926(3)	3133.3(3)
10.4(1)	10.014(1)	35.825(5)	3111.1(8)
10.76(1)	10.000(1)	35.814(5)	3101.6(5)
11.18(1)	9.989(1)	35.749(4)	3089.3(4)
11.74(1)	9.970(1)	35.688(4)	3072.5(5)
12.72(1)	9.955(1)	35.616(5)	3056.7(5)
13.68(1)	9.938(1)	35.531(5)	3039.1(6)
14.32(1)	9.924(1)	35.512(6)	3029.0(7)
14.90(2)	9.918(1)	35.460(4)	3020.6(5)

Pressure was determined by the *EoS* of Au (Fei et al. 2007). The number in the parentheses represents one standard deviation in the right-most digit. The measurement at 0.0001 GPa was obtained after decompression.

Table 2 Parameters of the Birch-Murnaghan *EoS* derived for some phosphates

Chemical formula	Space group	K_0 (GPa)	K_0'	Reference
$Ca_9Mg(PO_4)_7(OH)$	*R3c*	79(4)	4.3(6)	This study
		81(1)	4.0 (fixed)	
$Ca_9NaMg(PO_4)_7$	*R3c*	87.3(32)	3.2(4)	Jia et al. 2020a
		81.6(10)	4.0 (fixed)	
β-$Ca_3(PO_4)_2$	*R3c*	79.5(20)	4.0 (fixed)	Zhai et al. 2010
γ-$Ca_3(PO_4)_2$	*R-3m*	100.2(13)	5.48(16)	Zhai et al. 2009
		113.1(12)	4.0 (fixed)	
$Sr_3(PO_4)_2$	*R-3m*	89.5(17)	6.57(34)	Zhai et al. 2011b
		104.4(12	4.0 (fixed)	
$Pb_3(PO_4)_2$	*R-3m*	89(4)	5.8(2)	Qin et al. 2014
$Ca_5(PO_4)_3F_{0.94}Cl_{0.06}$	$P6_3/m$	91.5(38)	4.0(11)	Matsukage et al. 2004
		91.6(10)	4.0 (fixed)	
$Ca_5(PO_4)_3F$	$P6_3/m$	93(4)	5.8(18)	Comodi et al. 2001
		97.8(10)	4.0 (fixed)	
$Ca_5(PO_4)_3(F_{0.975},OH_{0.025})$	$P6_3/m$	97.9(19)	4.0 (fixed)	Brunet et al. 1999
$Ca_5(PO_4)_3OH$	$P2_1/b$	97.5(18)	4.0 (fixed)	Brunet et al. 1999
$Ca_5(PO_4)_3(Cl_{0.7},OH_{0.3})$	$P2_1/b$	93.1(42)	4.0 (fixed)	Brunet et al. 1999

Table 3 Frequencies of Raman modes, corresponding pressure/temperature derivatives, isobaric mode Grüneisen parameters, isothermal mode Grüneisen parameters, and intrinsic anharmonic parameters of whitlockite

Modes	v_{i0} at ambient conditions (cm^{-1})	$(\partial v_i/\partial P)_T$ (cm^{-1} GPa^{-1})	γ_{iT}	$(\partial v_i/\partial T)_P$ (cm^{-1} K^{-1})	γ_{iP}	β_i (10^{-5} K^{-1})
PO_4 modes						
v_3	1093	5.25(6)	0.38	-0.045(2)	1.02	-2.60
	1064	4.62(18)	0.34	-0.028(2)	0.65	-1.26
	1025	4.84(5)	0.37	-0.038(4)	0.92	-2.23
v_1	989	4.63(4)	0.37	-0.015(1)	0.37	0
	971	4.47(1)	0.36	-0.017(1)	0.42	-0.24
	961	3.40(1)	0.28	-0.017(1)	0.43	-0.61
	920	4.21(1)	0.36	-0.039(1)	1.05	-2.79
v_4	625	1.62(3)	0.20	-0.017(1)	0.66	-1.86
	604	1.79(13)	0.23	-0.010(1)	0.39	-0.65
	560	1.38(2)	0.19	-0.008(2)	0.37	-0.73
v_2	485	2.88(5)	0.47	-0.016(3)	0.82	-1.42
	460	2.27(9)	0.39	-0.010(4)	0.56	-0.69
	430	3.89(9)	0.74	-0.012(1)	0.68	0.24
	405	2.65(1)	0.52	-0.006(1)	0.34	0.69
External modes						
	280	1.26(6)	0.36	-0.049(5)	4.25	-15.80
	160	1.06(8)	0.52	-0.011(1)	1.73	-4.90

Table 4 Unit-cell parameters and volume of whitlockite at various temperatures

T(K)	*a*(Å)	*c* (Å)	*V*(Å^3)
306	10.3564(1)	37.1247(7)	3448.3(1)
373	10.366(1)	37.1684(7)	3458.7(1)
473	10.3798(1)	37.2393(7)	3474.6(1)
573	10.3904(1)	37.2970(6)	3487.2(1)
673	10.4032(1)	37.3720(5)	3502.8(1)
773	10.4159(1)	37.4464(5)	3518.3(1)
873	10.4242(1)	37.4998(5)	3528.9(1)
973	10.4277(1)	37.6147(5)	3542.1(1)

Values in parentheses are errors

Table 5 Thermal expansion coefficients for whitlockite and comparison with other phosphate minerals

Mineral	Formula	α_V ($\times 10^{-5}$ K^{-1})	α_a ($\times 10^{-5}$ K^{-1})	α_c ($\times 10^{-5}$ K^{-1})	Reference
whitlockite	$Ca_9Mg(PO_4)_7(OH)$	4.05(8)	1.07(5)	1.91(6)	This study
	β-$Ca_3(PO_4)_2$	3.35			Zhai et al. 2014
merrillite	$Ca_9NaMg(PO_4)_7$	4.86(5)	1.46(1)	1.94(5)	Jia et al.2020b
tuite	γ-$Ca_3(PO_4)_2$	3.67(3)	1.18(1)	1.32(3)	Zhai et al. 2011a
hydroxyapatite	$Ca_5(PO_4)_3OH$	3.95(5)	1.36(2)	1.24(2)	Hovis et al. 2014
fluorapatite	$Ca_5(PO_4)_3F$	3.70(10)	1.25(3)	1.22(4)	Chernorukov et al. 2011
		3.85(4)	1.30(1)	1.26(1)	Hovis et al. 2015
chlorapatite	$Ca_5(PO_4)_3Cl$	3.80(3)	0.91(8)	1.98(3)	Hovis et al. 2015

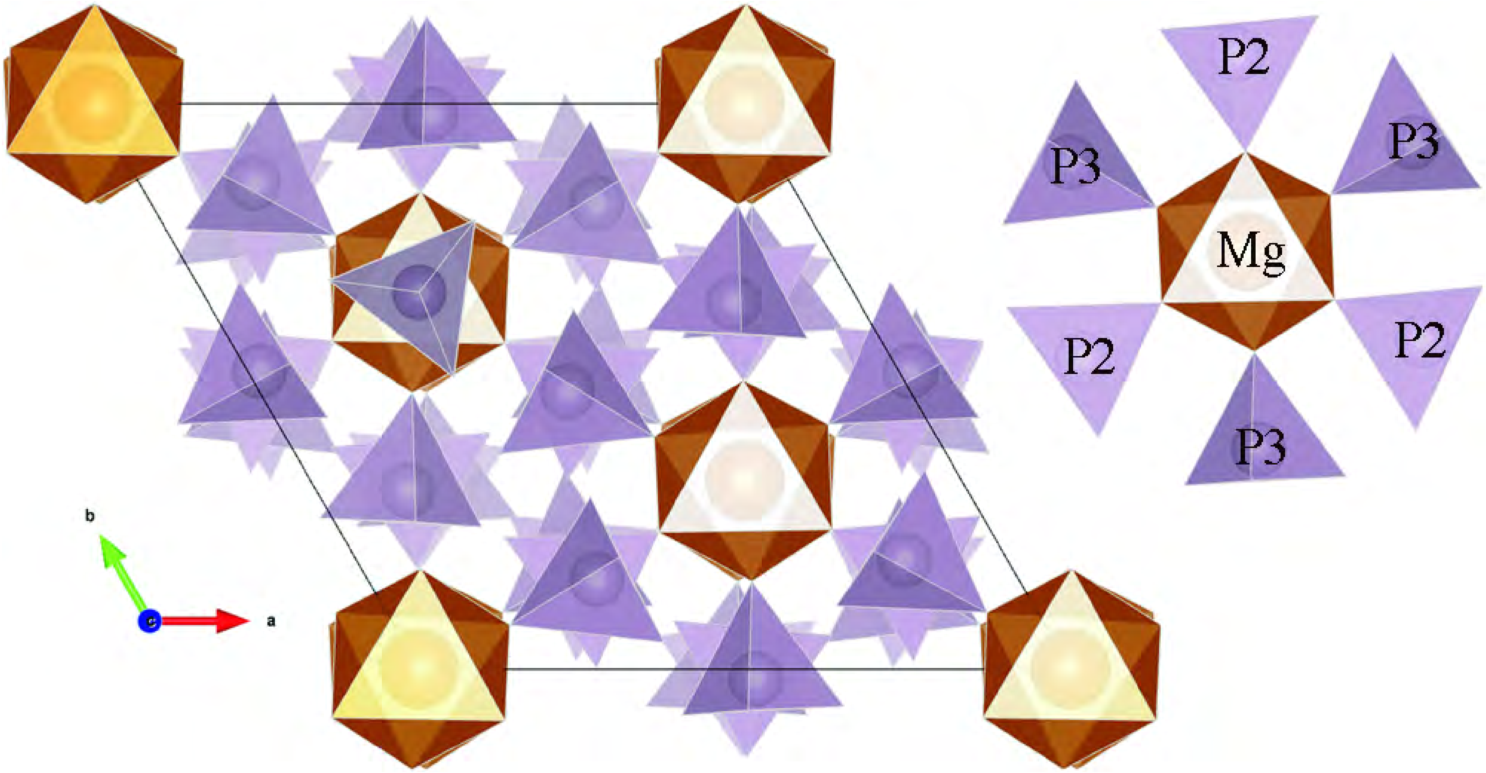
b
a
c
P2
P3
P3
Mg
P2
P2
P3

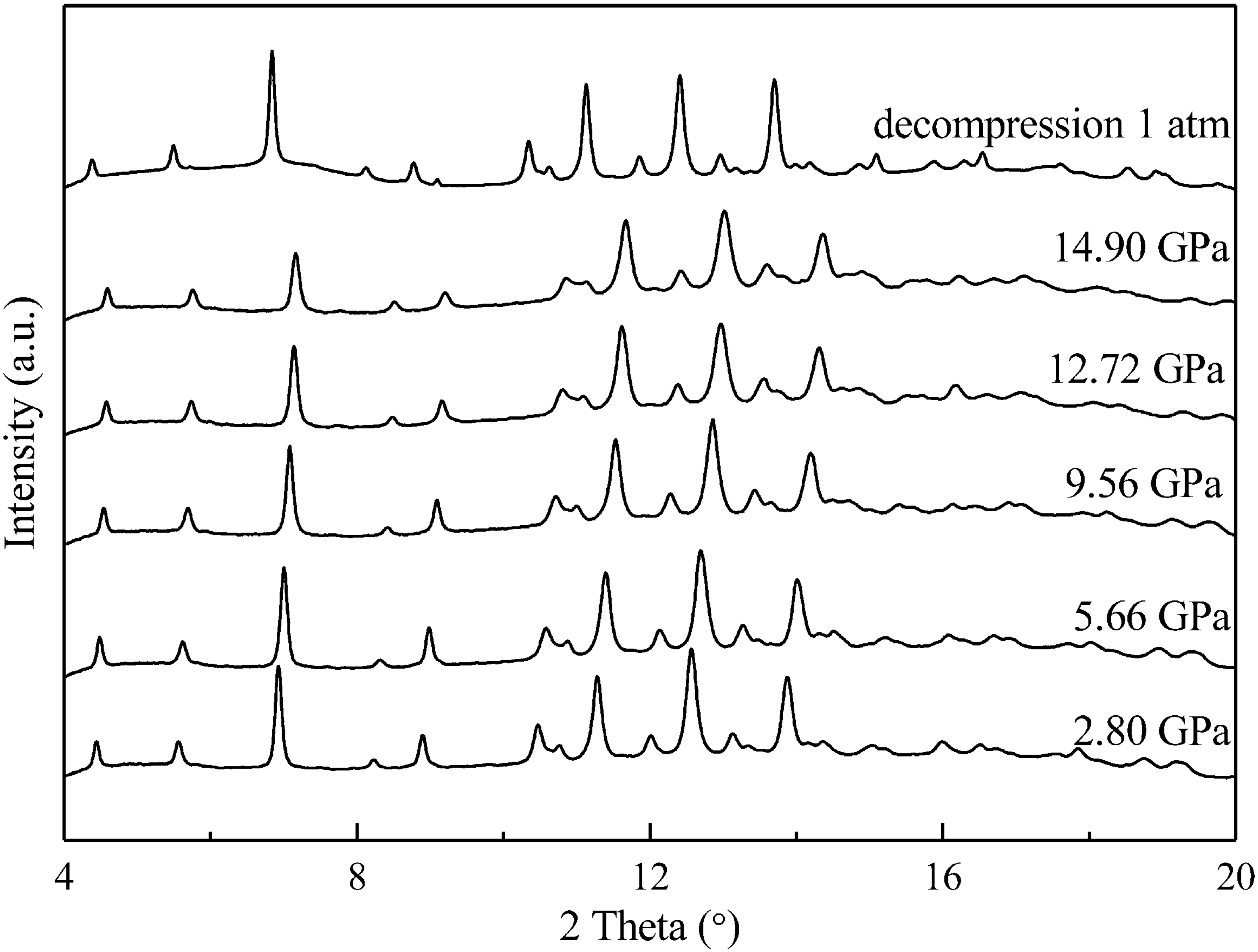
decompression 1 atm
14.90 GPa
12.72 GPa
9.56 GPa
5.66 GPa
2.80 GPa
Intensity (a.u.)
4
8
12
16
20
2 Theta (°)

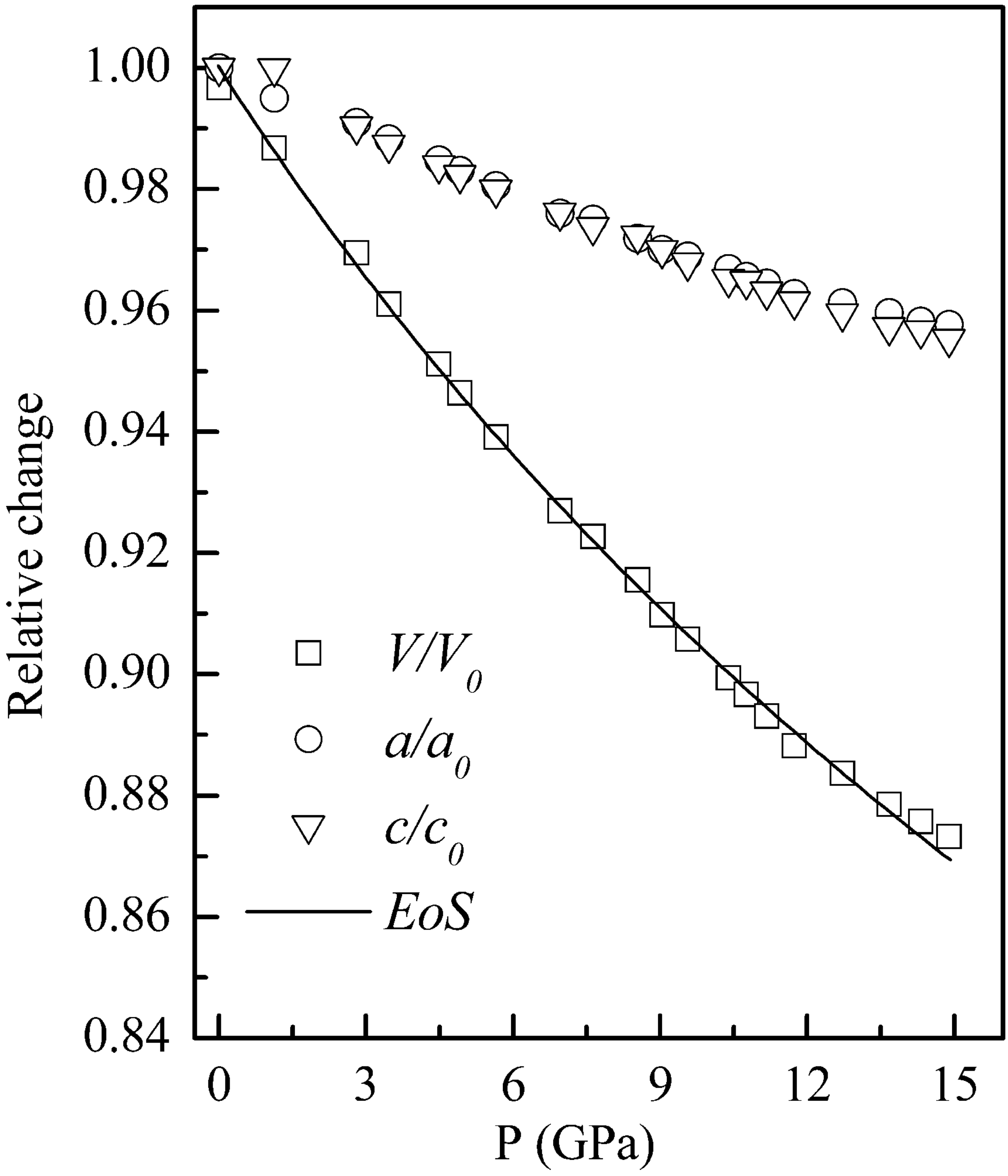
1.00
0.98
0.96
0.94
0.92
0.90
0.88
0.86
0.84
Relative change
0
3
6
9
12
15
P (GPa)
□ V/V0
○ a/a0
▽ c/c0
EoS

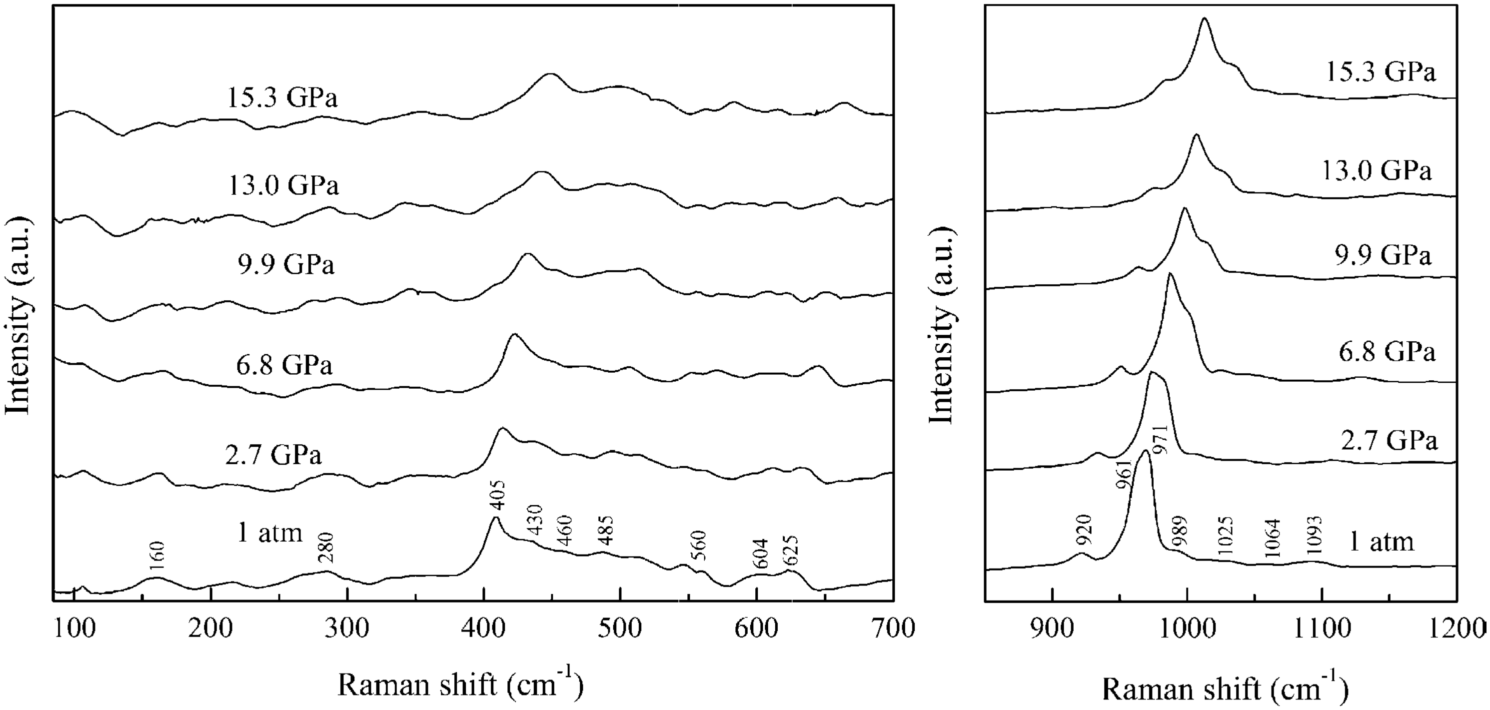
15.3 GPa
13.0 GPa
9.9 GPa
6.8 GPa
2.7 GPa
1 atm
160
280
405
430
460
485
560
604
625
Intensity (a.u.)
100
200
300
400
500
600
700
Raman shift (cm^{-1})
15.3 GPa
13.0 GPa
9.9 GPa
6.8 GPa
2.7 GPa
1 atm
920
961
971
989
1025
1064
1093
Intensity (a.u.)
900
1000
1100
1200
Raman shift (cm^{-1})

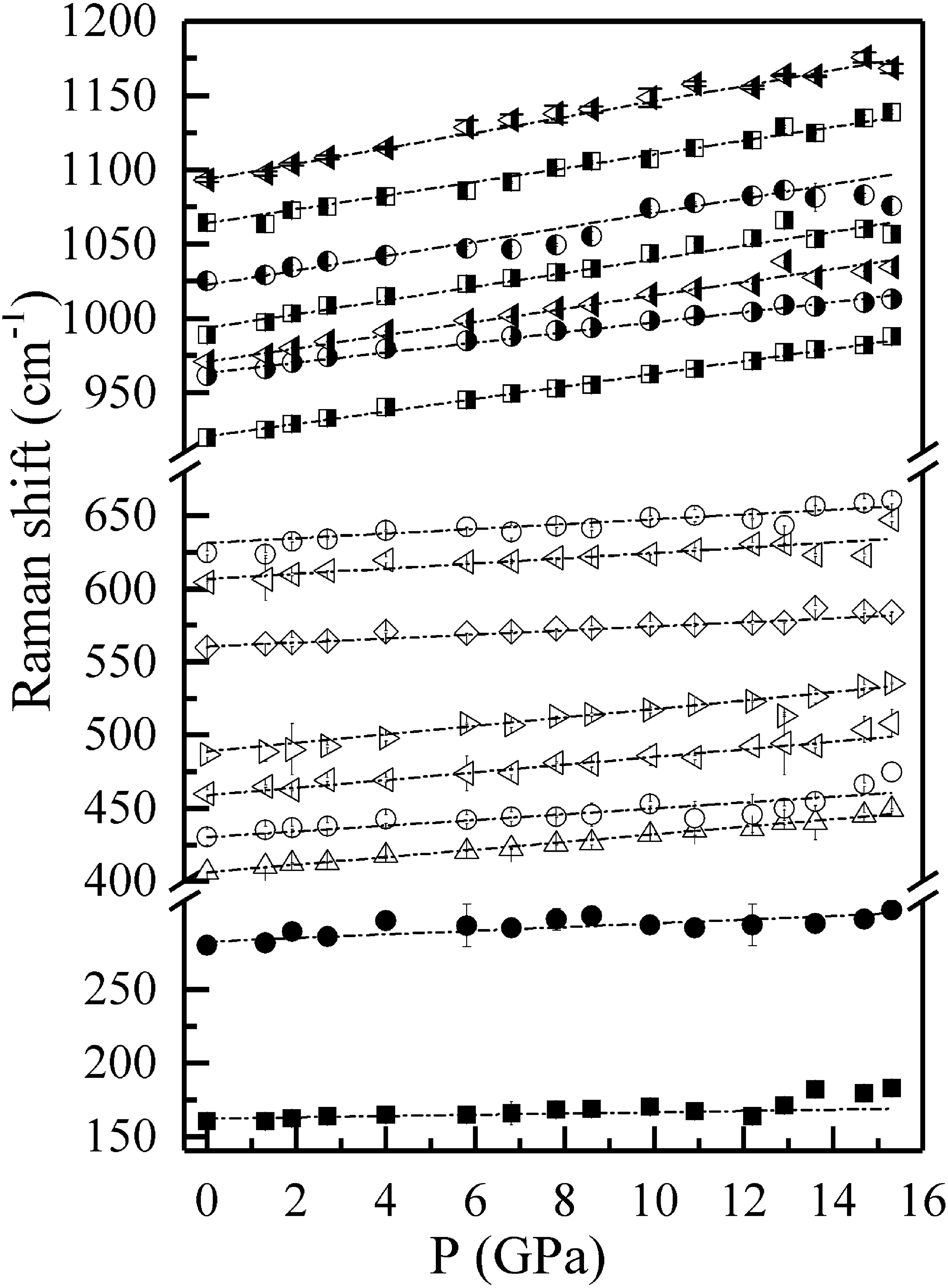
1200
1150
1100
1050
1000
950
650
600
550
500
450
400
250
200
150
Raman shift (cm^{-1})
0
2
4
6
8
10
12
14
16
P (GPa)

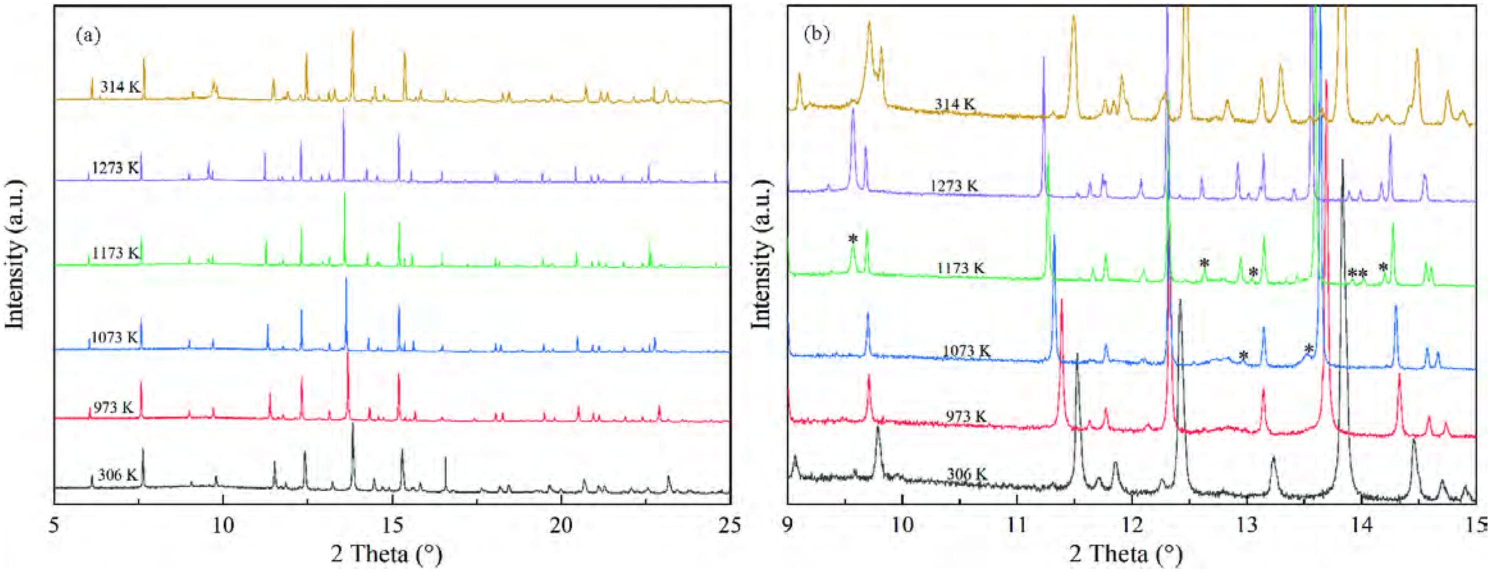
(a)
314 K
1273 K
1173 K
1073 K
973 K
306 K
Intensity (a.u.)
5
10
15
20
25
2 Theta (°)
(b)
314 K
1273 K
1173 K
1073 K
973 K
306 K
*
Intensity (a.u.)
9
10
11
12
13
14
15
2 Theta (°)

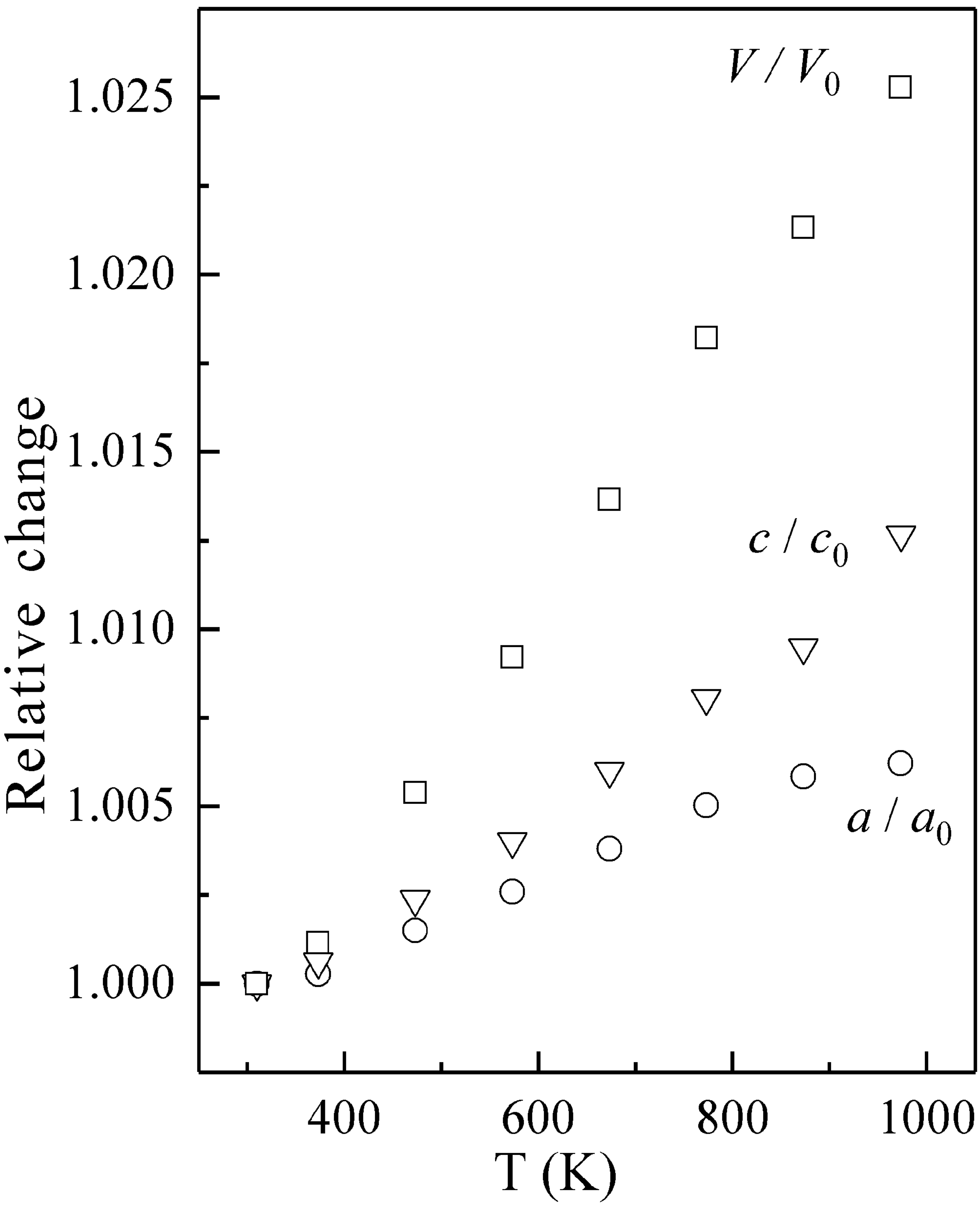
V / V_0
c / c_0
a / a_0
Relative change
1.025
1.020
1.015
1.010
1.005
1.000
400
600
800
1000
T (K)

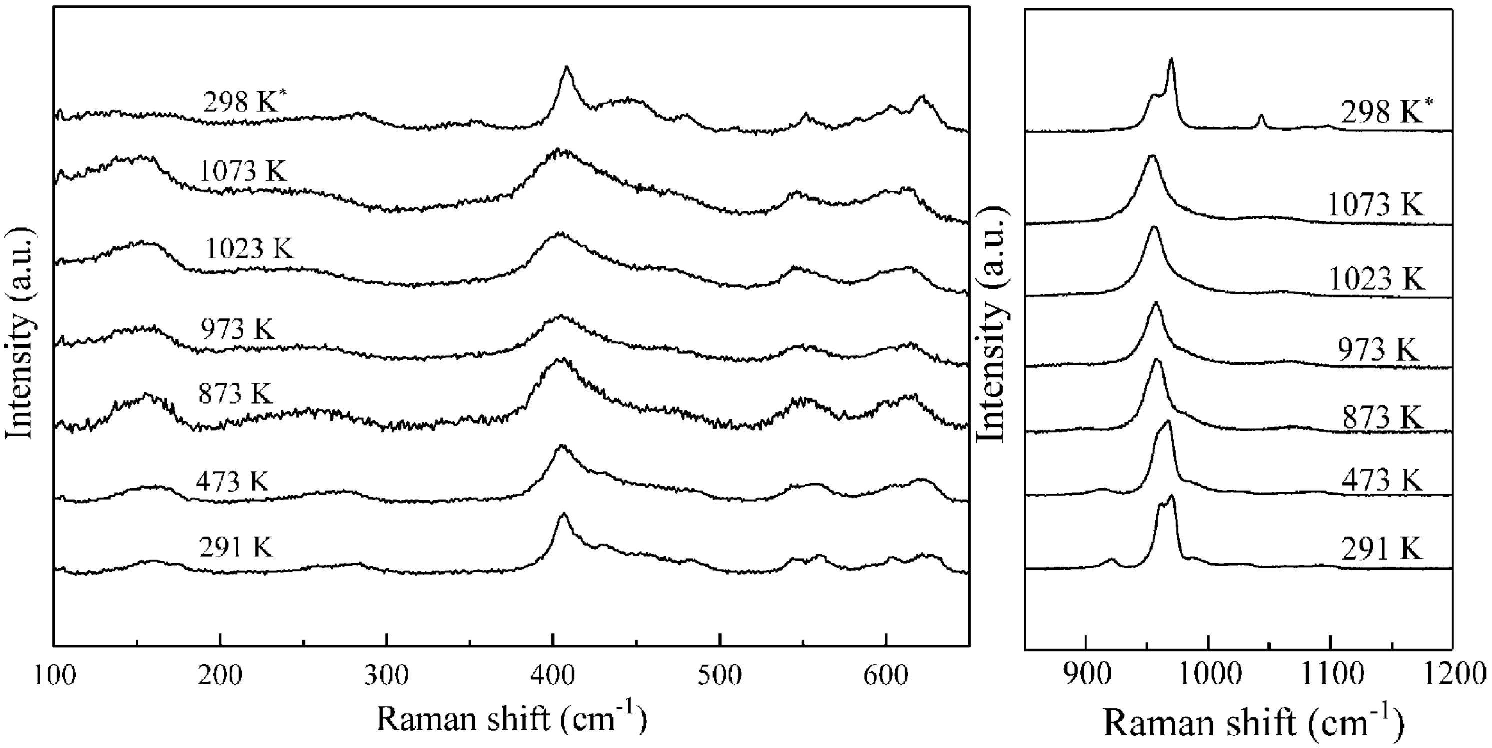
298 K*
1073 K
1023 K
973 K
873 K
473 K
291 K
Intensity (a.u.)
Raman shift (cm-1)
100
200
300
400
500
600
900
1000
1100
1200

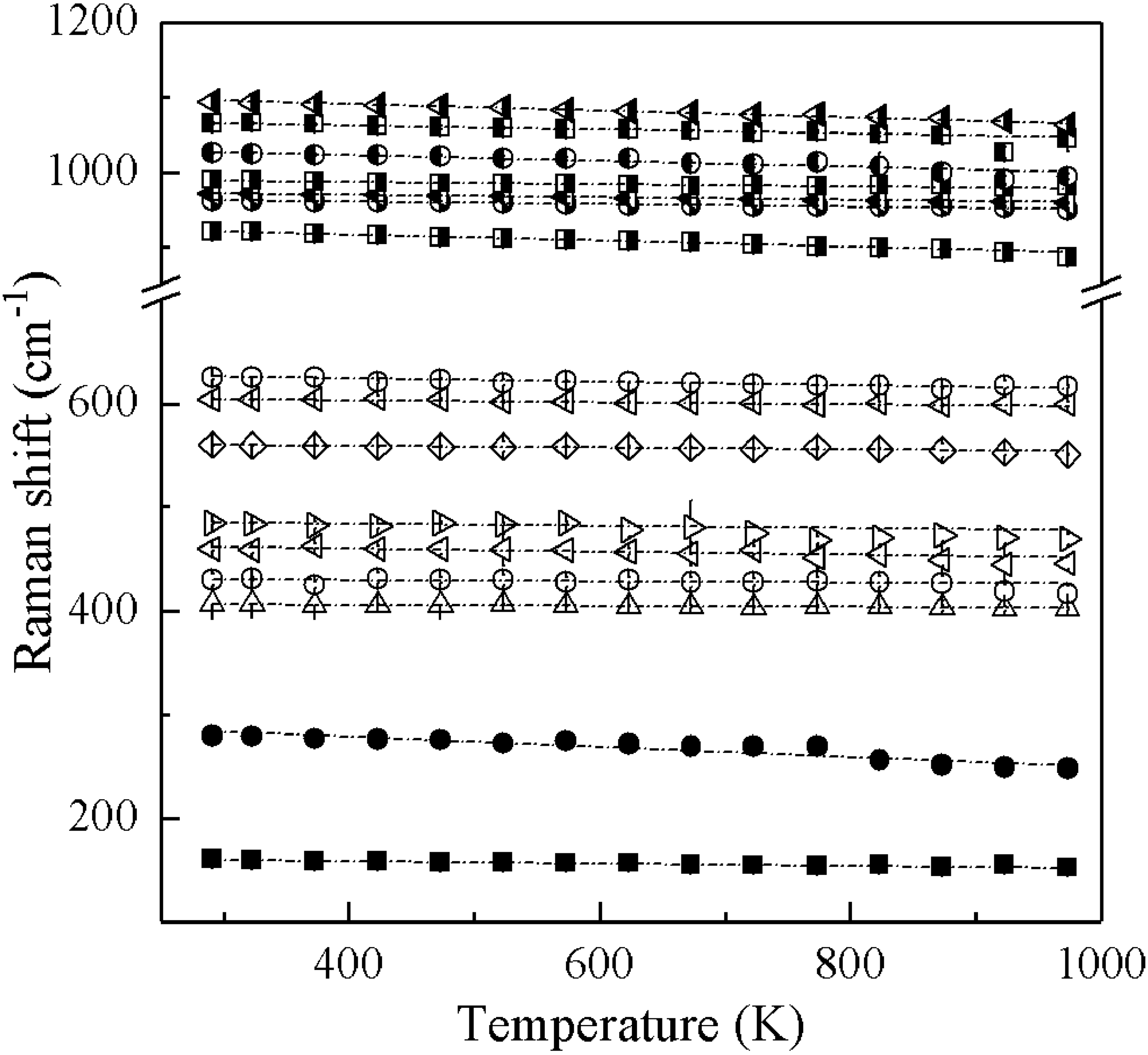
1200
1000
600
400
200
Raman shift (cm^{-1})
400
600
800
1000
Temperature (K)